

FastPillars: A Deployment-friendly Pillar-based 3D Detector

Sifan Zhou¹, Zhi Tian², Xiangxiang Chu², Xinyu Zhang², Bo Zhang², Xiaobo Lu^{1*},
Chengjian Feng², Zequn Jie², Patrick Yin Chiang³, Lin Ma²,

¹ Southeast University ² Meituan Inc. ³ Fudan University

sifanjay@gmail.com, tianzhi02, chuxiangxiang, zhangxinyu35, zhangbo97@meituan.com

xblu2013@126.com, fengchenhgjian, jiezequn, malin11@meituan.com, pchiang@photonic-tech.com

Abstract

The deployment of 3D detectors strikes one of the major challenges in real world self-driving scenarios. Existing BEV-based (i.e., Bird Eye View) detectors favor sparse convolution (known as SPConv) to speed up training and inference, which puts a hard barrier for deployment especially for on-device applications. In this paper, we tackle the problem of efficient 3D object detection from LiDAR point clouds with deployment in mind. To reduce computational burden, we propose a pillar-based 3D detector with high-performance from an industry perspective, termed FastPillars. Compared with previous methods, we introduce a more effective Max-and-Attention pillar encoding (MAPE) module, and redesigning a powerful and lightweight backbone CRVNet imbued with Cross Stage Partial network (CSP) in a reparameterization style, forming a compact feature representation framework. Extensive experiments demonstrate that our FastPillars surpasses the state-of-the-art 3D detectors regarding both on-device speed and performance. Specifically, FastPillars can be effectively deployed through TensorRT, obtaining real-time performance (~ 24 FPS) on a single RTX3070Ti GPU with 64.6 mAP on the nuScenes test set. Our code will be released.

1. Introduction

3D object detection using LiDAR point cloud has a wide range of applications in autonomous driving and robotics [27, 32, 41]. Compared to RGB images, 3D point cloud is less sensitive to illumination changes and could accurately represent the geometric information of a scene. However, LiDAR-based 3D object detection has their own challenges. First, different from an image which is a regular matrix, point cloud is irregular and disordered [28]. Second, unlike a dense image, point cloud is sparse and spatially discrete, especially the points far away from the ego. Third, 3D ob-

ject detection needs to estimate higher space dimension information (e.g., 3D-location, 3D-size, orientation) than 2D detection, which make it significantly more complicated.

One of the mainstream methods [26, 31, 33, 45] directly learns discriminative representation from raw point cloud without converting it into volumetric grids. In these methods, symmetric functions [28, 29] are leveraged to cope with the orderless of points. Although these methods retain the original geometry information of point cloud as much as possible, these methods might not be friendly to effective hardware implementation as they often require point query/retrieval in 3D space (e.g., PointNet++ [29]). Voxel-based 3D detectors [24, 49] are another mainstream solution. In these methods, the irregular point cloud is first transformed into arranged grids (i.e., voxels), and then 2D/3D CNN is used to extract features. After the voxelization process, many empty grids will be generated due to the sparsity of the point cloud, which will lead to great redundant computational overheads. In order to improve computational efficiency, some methods [6, 10, 30, 44, 47] use 3D sparse convolution [14] to skip convolution calculation on empty grids. Despite being effective, sparse convolution poses a challenge when converted to ONNX/TensorRT for deployment and network quantization and hampers further speedup through these techniques. These techniques often speed up the model inference by several times and are extensively used in industrial deep learning model deployment, particularly on resource-constrained platforms.

Currently, one of the popular methods for on-device deployment is PointPillars [19]. In this method, the point cloud is first converted into pillars (i.e., only voxelization in the plane), and then they utilize PointNet [28] to learn the features of points in each pillar. Afterwards, a mature 2D detector pipeline is applied to predict 3D bounding boxes. This method only adopts 2D convolutions, making it easy to be converted into ONNX/TensorRT for deployment and take advantage of the network quantization with various precisions FP32/FP16/Int8, meeting the requirements of different embedded platforms. However, PointPillars

*Corresponding author.

simply leverages a max-pooling operation to aggregate all point features in a pillar, which decimates much local fine-grained information and impairs performance, especially for small objects. Besides, based on the feature pyramid network (FPN [22]), PointPillars directly fuses multi-scale features with strides of $1\times$, $2\times$ and $4\times$ but lacks sufficient feature interaction between different layers. Although PointPillars has great advantages in speed, its performance still lags far behind other methods, *e.g.*, [47]. To boost the performance of pillar-based method, PillarNet [30] was proposed and it can achieve high-performance 3D detection performance while keeping real-time. PillarNet uses a sparse convolution-based encoder network for spatial feature learning and a neck module for high-level and low-level feature fusion. Nevertheless, the use of SPConv in PillarNet makes it hard to be quantified and deployed via TensorRT. Specifically, SPConv takes as inputs 3D coordinates that are difficult to be quantized. Moreover, if we want to use commonly-used TensorRT for the quantization deployment, SPConv is not a built-in operation in TensorRT. Thus one needs to write a tedious custom plugin in CUDA C++ with several limitations like fixed-shape input and reduced compatibility. It also requires taking fusion into consideration for fast execution, further complicating the deployment process.

In this paper, we propose an efficient 3D object detector from LiDAR point cloud, termed **FastPillars**. FastPillars is fully based on standard convolutions, and thus it can be easily deployed in industrial applications and seamlessly enjoy the speedup of TensorRT and network quantization. **FastPillars** consists of four blocks which are for pillar encoding, feature extraction, feature fusion and 3D boxes regression, respectively. For pillar encoding, we propose a simple but effective Max-and-Attention Pillar Encoding (MAPE) module, which automatically learns local geometry patterns almost without additional latency (4 ms). The MAPE module attentively integrates important local features in each pillar, which significantly benefits the accuracy of small objects. For feature extraction, in order to enhance the representation ability of the model and reduce the computational burden for low-latency onboard deployment, we designed a compact and efficient backbone network, named CRVNet (Cross-Stage-Patial RepVGG-style Network). We draw our inspiration from the CSP (cross-stage-Patial) structure and reparameterized RepVGG network and proposes a compact network while maintaining strong feature extraction ability. Moreover, in the feature fusion block, the semantic features are enriched by fusing features from different levels and receptive fields hierarchically. For the regression module, we adopt an efficient center-based head to regress the score, dimension, location, rotation and box intersection over union (IOU) information of targets, respectively. Together with these components, we built our **Fast**

Pillars, which is a fully convolutional deployment-friendly pillar-based 3D detector. The proposed method achieves even better trade-off between speed and accuracy for real-time embedded applications. Additionally, extensive experiments show that FastPillars achieves state-of-the-art performance on the nuScenes dataset. In addition, it can be seamlessly speeded up through TensorRT to achieve a speed of 24 FPS. Our full codebase will be open-sourced to facilitate further research. We summarize our contributions as follows:

- We propose a pillar-based one-stage 3D detector for industrial applications, termed **FastPillars**. Our proposed method is deployment-friendly and eliminates the need for sparse convolutions hampering the on-device deployment. We propose two instantiations of our FastPillar, *i.e.*, FastPillar-*s* and FastPillar-*m*, which can achieve 64.6 mAP and 70.1 NDS with 24 FPS, and 66.0 mAP and 71.1 NDS with 16 FPS on the nuScenes test set, respectively.
- A simple but efficient Max-and-Attention Pillar Encoding (MAPE) module is also presented. MAPE can improve the representation ability of each pillar feature almost without additional latency (only ≈ 4 ms).
- We designed a compact fully convolutional backbone network CRVNet for 3D detection tasks, which has competitive feature learning ability and inference speed without the need for sparse convolutions. Meanwhile, we also show that the lightweight network structure specially designed for 2D images can work well on the tasks with 3D point cloud and achieve an excellent trade-off between performance and speed as well.
- Extensive experiments on the nuScenes dataset demonstrate that the superior efficiency and accurate detection performance of our FastPillars. We also provide a detailed performance vs. inference-speed analysis to further validate the superiority of our method.

2. Related Work

Voxel-based 3D Detectors. Voxel-based 3D detectors [5, 6, 18, 19, 30, 44, 47, 49] generally transform the unstructured point cloud to regular pillar/voxel grids in compact shapes. This further allows learning point features by leveraging the mature 2D/3D convolution neural networks. VoxelNet [49] is a pioneering work, which densely voxelizes the input point cloud and then utilizes Voxel Feature Extractor (VFE) and 3D CNNs to learn the geometrical representation. Its shortcoming is the relatively slow inference speed due to the huge computational burden of the 3D convolutions. To save the memory cost, SECOND [44] uses 3D sparse convolutions [14] to speed up the training and inference. Here, sparse convolution only operates on non-empty voxels, which greatly improves computational and

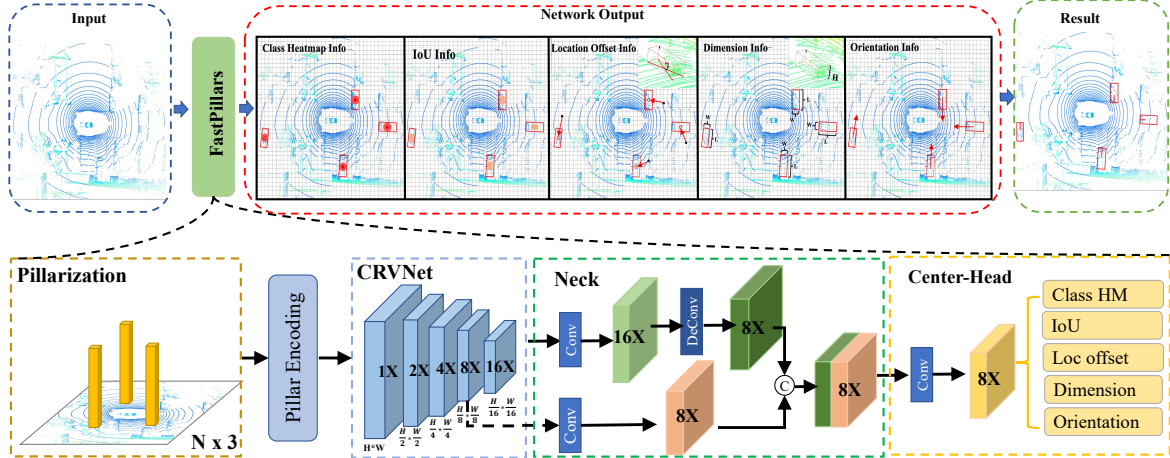


Figure 1. The overall network architecture of **FastPillars**. As shown in the top, taking the raw point cloud as inputs, **FastPillars** outputs the information of object classes, IoU, location offsets, dimension and heading angle information, and finally outputs the predicted 3D bounding boxes. As shown in the bottom, **FastPillars** consists of four parts: the pillar encoding module, a backbone, a neck and heads. In detail, the point cloud is firstly pillarization (one yellow column represents a pillar), and then all the columns are encoded, and the encoded features are sent to the CRVNet backbone for feature extraction. These features are fused by the neck, and finally, the heads similar to CenterPoint are applied for 3D box regression. Our CRVNet provides two optional backbone network variants, the CSPRepVGG backbone for FastPillars-*s* and the CSPRep-Res34 backbone for FastPillars-*m*. Best viewed in color.

memory efficiency. A drawback of SPConv is that it is not deployment-friendly, which makes it tricky to apply them on embedded systems. To this end, PointPillars [19] is proposed to further simplify the voxels to pillars (*i.e.*, without voxelization in height) and utilize highly-optimized 2D convolutions, which attains decent performance with low latency. Meanwhile, the advantage of being deployment-friendly makes PointPillars become a mainstream method in practice. After that, CenterPoint [47] is proposed, which uses a nearly real-time and anchor-free pipeline, achieving state-of-the-art performance. Recently, PillarNet [30] projects point to the BEV space and uses 2D SPConv based on the “encoder-neck-head” architecture to boost 3D detection performance in a real-time speed. Due to the use of SPConv, it inevitably faces the difficulty of deployment in industrial applications and further speedup with the network quantization.

Industry-level Lightweight Network Structures for Object Detection. For years, the YOLO series [1, 12] has been the *de facto* industry standard for lightweight 2D object detection, whose backbone designs mainly inherit the ideas from CSPNet [40]. By processing partial features in two separate branches to have a richer gradient combination, CSPNet not only reduces the memory and computational costs but also improves performance.

Most recently, RepVGG [8] refactored the famous plain network VGG [34] using a reparameterization-based structural design. During training, a plain Conv-BN-ReLU is replaced by its over-parameterized three-branch counter-

part, *i.e.*, Conv3×3-BN, Conv1×1-BN and Identity-BN, followed by the ReLU function after the summation of the three branches. The three-branch structure substantially helps the network optimization while the reparameterization converts three branches identically into one at inference, improving the efficiency in inference. Due to this advantage, this trend has swept 2D object detectors and shown high performance at extreme speeds, such as PPYOLO-E [43], YOLOv6 [21] and YOLOv7 [39]. Albeit the success, it is not yet seen, to our best knowledge, any application of these schemes in 3D detection.

3. Our Approach

In this section, we introduce FastPillars for real-time pillar-based one-stage 3D object detection, which is an end-to-end trainable and SPConv-free neural network. As shown in Fig. 1, our network architecture consists of four parts: the pillar encoding module, a backbone for feature extraction, a neck for feature fusion and a head for 3D boxes regression. We introduce each block in detail in the remainder of this section.

We present the basic task definitions of LiDAR-based 3D detection before introducing the detailed method. Given a point set with N points in the 3D space, which is defined as $\mathbf{P} = \{\mathbf{p}_i = [x_i, y_i, z_i, r_i, t_i]^T \in \mathbb{R}^{N \times 5}\}$, where x_i, y_i, z_i denote the coordinate values of each point along the axes X, Y, Z, respectively, and r_i is the laser reflection intensity. t_i is the relative timestamp, which is optional and depends on the specific settings of a dataset. Given a set of object in the 3D scene $\mathbf{B} = \{\mathbf{b}_j = [x_j, y_j, z_j, h_j, w_j, l_j, \theta_j, c_j]^T \in \mathbb{R}^{N \times 8}\}$

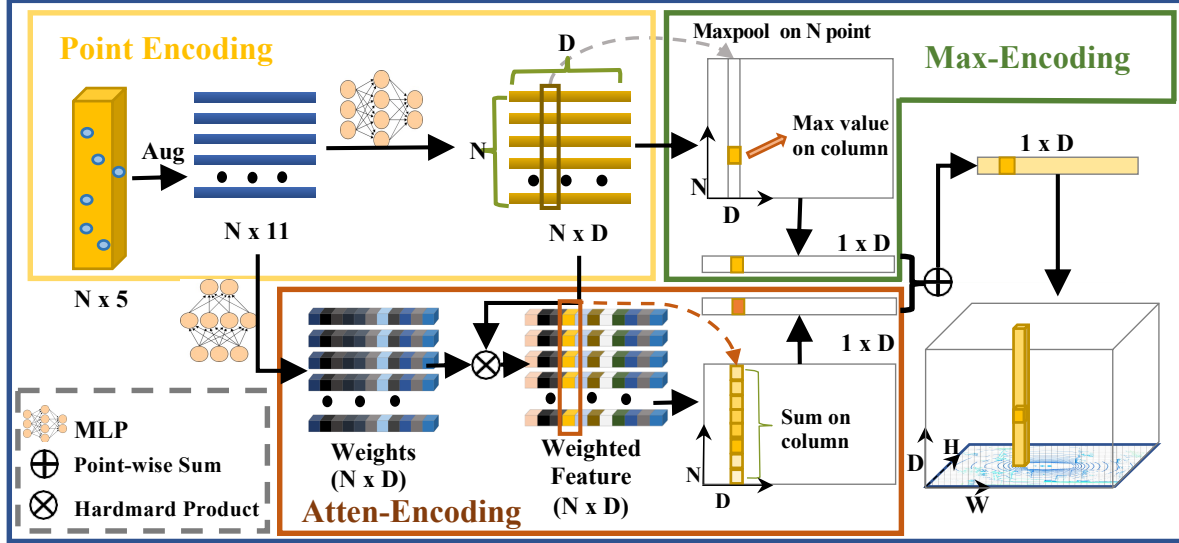


Figure 2. Our Max-and-Attention Pillar Encoding (MAPE) module architecture. It consists of three units: point encoding, max-pooling encoding and attentive-pooling encoding. The input of this module is raw point cloud containing N points after the pillarization as an example. In the point encoding unit, the raw points are firstly augmented by the information of the pillar center and point cloud range, then the augmented point features are mapped to the feature space by an MLP. In the max-encoding unit, pillar-wise features are represented by a max-pooling operation across these point features. In the attentive-encoding unit, pillar-wise features are represented by a weighted summation operation on these point features. Finally, the current pillar feature is obtained by averaging the max-pool and attentive-pool features.

$\mathbb{R}^{M \times 5}$ }, where M is the total number of objects, b_i is the j -th object in the scene, x_j, y_j, z_j is the object's center, h_j, w_j, l_j is the object's size, θ_j is the object's heading angle and c_j is the class of the object. The task of 3D object detection is to detect the 3D boxes \mathbf{B} from the point cloud \mathbf{P} accurately.

3.1. Max-and-Attention Pillar Encoding

Point cloud voxel/pillar encoding is very crucial for grid-based 3D detection methods. The pioneering PointPillars [19] aggressively utilizes max pooling to aggregate point features in each pillar to represent the corresponding pillar. However, the max-pooling operation will result in the loss of fine-grained information, and those local geometric patterns are very crucial for pillar-based objects, especially for small objects. In this paper, we propose a simple but efficient pillar encoding module, named **Max-and-Attention Pillar Encoding (MAPE)**, which takes into account every pillar's local detailed geometric information with negligible computational burden and benefits the performance of small objects (*e.g.*, pedestrians and etc.) in BEV. Meanwhile, the lightweight pillar encoding method of our MAPE module makes it highly suitable for real-time embedded applications. As shown in Fig. 2, our MAPE module consists of three units: 1) the point encoding unit, 2) the max-pooling encoding unit, 3) and the attentive-pooling encoding unit.

We suppose that a point cloud \mathbf{P} in the 3D space has the range of L, W, H along the axes X, Y, Z. \mathbf{P} is equally

divided into a specific pillar grid with the size of v_L, v_W, H . Here, as in PointPillar, we only voxelize point cloud in the XY plane without the height dimension. Let $v = \{p_i = [x_i, y_i, z_i, r_i, t_i] \in \mathbb{R}^{N \times 5}\}$ be a non-empty pillar comprising N_i points with the spatial shape $[v_L, v_W, H]$, i is the index of the pillar.

Point Encoding. First, we augment the points in each pillar into $\hat{p}_i = \{[x_i, y_i, z_i, r_i, t_i, x_i^c, y_i^c, z_i^c, x_i^r, y_i^r, z_i^r] \in \mathbb{R}^{N \times 11}\}$, where $[x_i, y_i, z_i]$ is the original point coordinates in the ego frame, $[x_i^c, y_i^c, z_i^c]$ is the offset of p_i from the current pillar center, and $[x_i^r, y_i^r, z_i^r]$ is the relative coordinates of p_i obtained by subtracting the minimums of point cloud from it. Notably, in each pillar, we did not adopt any sampling strategy to keep the number of points within each the same, because this operation may drop useful points and impair the original geometric patterns. Second, the augmented point-wise features \hat{p}_i within v are mapped to the high-dimensional feature space through an MLP layer. This process is formulated as

$$p_i^e = m(\hat{p}_i; w_m), \quad (1)$$

where function $m(\cdot)$ denotes a stack of multiple MLP layers with Batch Normalization (BN) layers and Leaky Rectified Linear Unit (LeakyReLU) layers, w_m denotes learnable weights of function $m(\cdot)$, and $p_i^e \in \mathbb{R}^{N \times D}$ is point-wise feature.

Max-pooling Encoding. This unit is used to aggregate all point features inside a pillar into a single feature vec-

tor while it is invariant to point permutations in each pillar, which is formulated as

$$f^m = \max(p_i^e), \quad (2)$$

where $\max(\cdot)$ means the max-pooling operation across these point features, and $f^m \in \mathbb{R}^D$ is the resulting feature vector of each pillar.

Attention-pooling Encoding. This unit is designed to maintain the local fine-grained information. Max pooling is hard to integrate point-wise features p_i^e within each pillar v as it only takes the maximum. However, the rich local detailed patterns are very useful for smaller object detection from BEV perspective. Therefore, we turn to the powerful attention mechanism to automatically learn the important local features. To be specific, **first**, we use a function $g(\cdot)$ consisting of a shared MLP to predict attention scores for these points in a pillar, *i.e.*, $s_i = g(p_i^e; w_g)$, where w_g denotes learnable weights of the MLP, $s_i \in \mathbb{R}^{N \times D}$ the attentive scores. **Second**, the learnt attention scores can be regarded as a soft mask which dynamically weigh the point-wise feature p_i^e . Finally, the weighted summed features are as follows:

$$f^a = \sum_i \frac{s_i \cdot p_i^e}{\sum_j s_j}, \quad (3)$$

where $f^a \in \mathbb{R}^D$ is resulting pillar attentive pooling features.

Finally, we combine the learnt pillar-wise max-pool and attentive pooling features by averaging them, *i.e.*, $f = \frac{f^m + f^a}{2}$, where $f \in \mathbb{R}^D$ is the final pillar-wise feature including the global-aware and local-aware information inside one pillar. The max-pooling operation preserves the maximum response feature in each pillar, while the attentive pooling features maintain the local fine-grained information. By combining the two features, more rich information can be effectively retained to enhance the pillar representation. Despite being a simple method, our MAPE module significantly affects the performance of small objects as shown in our experiments. Notably, the MAPE module improves approximately 0.6 mAP performance on the nuScenes dataset only with an extra 4 ms latency.

3.2. CRVNet Backbone

The backbone network aims to extract various levels of semantic features hierarchically from the projected 2D pseudo-image or 3D voxel feature. Previous works [6, 30, 44, 47] generally use sparse convolution [14] to extract voxel/pillar-wise feature based on the ResNet [15] or VGG [34] architecture. Sparse convolution greatly improves the computational efficiency because most of the voxels/pillars are empty. For example, the proportion of empty pillars is approximately 90% in a single frame point cloud on the nuScenes dataset. However, using 2D convolution directly

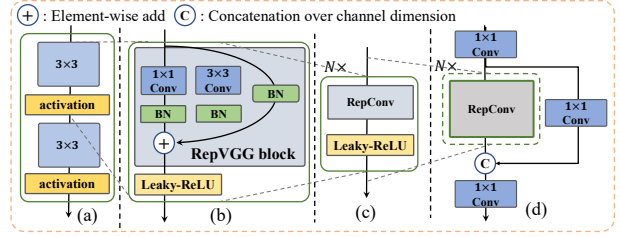


Figure 3. The architecture of CRVNet. CRVNet consists of CSP and RepVGG-style structures. Here we take VGG network as an example. (a) RepBlock is composed of a stack of RepVGG blocks with the activation functions at training. (b) During inference time, RepVGG block is converted to RepConv. (c) There are N RepConvs modules in each RepVGG stage. (d) CSPRep Block comprises three 1×1 convolutional layers and a stack of sub-blocks of N RepConvs followed by the activation functions with a residual connection.

on the sparse feature map will lead to excessive computation burden and high latency, which motivates us to design a more compact and effective backbone network.

Inspired by RepVGG [8] and CSPNet [40], we proposed CRVNet (Cross-Stage-Paternal RepVGG-style Network). The main components of our network are shown in Fig. 3. Each block during the training stage is shown in Fig. 3 (a). In the inference stage (Fig. 3 (b)), each RepBlock is converted into a stack of 3×3 convolutional layers (denoted as RepConv) with an activation function. This is because a 3×3 convolution has a higher computational density and is highly efficient on most devices. As a result, the RepBlock backbone network significantly reduces the inference latency with excellent feature representation ability. Besides, we notice that if the model capacity is expanded further, the computational cost and the number of parameters in the single-path plain network increase exponentially. Therefore, we further incorporated RepBlock with the CSP structure. As shown in Fig. 3 (d), the CSP structure is composed of three 1×1 convolutional layers and the original network structure. We use the CSP structure at each stage of the backbone network, where each stage contains N RepConvs (Fig. 3 (c)). By introducing the CSP structure, the whole network has fewer parameters and is more compact and efficient. Notably, although RepBlock and CSP prove effective in 2D image-based tasks [21, 39, 43], they have not yet been fully exploited for the 3D point cloud tasks. Our FastPillars-*s* and FastPillars-*m* models are built on VGG and ResNet-34 network, respectively. We found that the final performance is not sensitive to the capacity of the later stages but quite sensitive to that of the early stages, which is consistent with the situation in FCOS-LiDAR [36]. Therefore, we change the numbers of blocks of VGG’s four stages from (4, 6, 16, 1) to (6, 16, 1, 1) in FastPillars-*s* and the numbers of blocks of ResNet-34’s four stages from

(3, 4, 6, 3) to (6, 6, 3, 2) in FastPillars-*m* while both removing the first 2× downsampling in the first stage.

3.3. Neck and Center-based Heads

In the neck block, we adopt the enriched neck design as in PillarNet [30]. The neck module fuses the features with 8× and 16× features maps from the backbone to implement the effective interaction of different spatial semantic features. We find that in this neck design, the number of convolutional layers before the concatenation operation significantly affects the final performance. We will discuss this in detail in our experiment. For the regression head, we directly follow [47] to use their simple but effective head design. Besides, we also add an IoU branch to predict the 3D IoU between the predicted boxes and ground-truth boxes. Then, the IoU-Aware rectification function in [17] is used to bridge the gap between the classification and regression prediction. Specifically, the rectified confidence scores C for non-maximum suppression (NMS) post-processing are computed by

$$C = S^{1-\alpha} + I^\alpha, \quad (4)$$

where S is the predicted classification scores, I is the predicted IoU values, and $\alpha \in [0, 1]$ is a hyper-parameter that balances the contribution of S and I .

3.4. Loss Functions

We follow [47] to design our loss functions. To be specific, for the classification branch, we use the focal loss [23] as the heatmap loss \mathcal{L}_{cls} . For the 3D box regression, we make use of the L1 loss \mathcal{L}_{reg} to supervise their localization offsets, size and orientation. For the IoU branch, we also utilize the L1 loss \mathcal{L}_{iou} to supervise, where the target 3D IoU score I is $2 \times (I - 0.5) \in [-1, 1]$. Besides, following [30], the DIoU loss \mathcal{L}_{od-iou} [48] is added in the regression branch. The overall loss consists of four parts as follows:

$$\mathcal{L}_{total} = \lambda_1 \mathcal{L}_{cls} + \lambda_2 \mathcal{L}_{iou} + \lambda_3 (\mathcal{L}_{od-iou} + \mathcal{L}_{reg}), \quad (5)$$

where λ_1 , λ_2 , and λ_3 represent the balance weights of these losses as in [47].

4. Experiments

Dataset. We evaluated our method on the nuScenes dataset [2]. The Nuscenes dataset contains 1000 scenarios, with 700 training sequences, 150 val sequences and 150 test sequences scenes. The nuScenes dataset uses a LiDAR with 32 channels that generates approximately 30K points per frame. The training, validation and testing set have 28K, 6K and 6K annotated keyframes, respectively. It contains 10 categories in total. Its main ranking metric is the nuScenes detection score (NDS), which is a weighted

average of mAP, the translation error, the scale error, the orientation error, the velocity error, and the box attributes error. The Mean Average Precision (mAP) [9] was also used based on distances between the centers of the predictions and ground-truths on the bird-eye view at thresholds 0.5m, 1m, 2m, and 4m.

Implementation Details. FastPillars is trained by 20 epochs with the Adam optimizer under the Det3D [50] framework, which takes~25 hours on 8 A100 GPUs with batch size 32. For speed test, we compare our method with the baselines. The one-cycle learning rate policy [35] with an initial learning rate 10e-4 is used. The learning rate gradually increases to 0.001 in the first 40% epochs and then gradually decreases to 10e-5 in the rest of the training process. The weight decay is 0.01, and the momentum ranges from 0.85 to 0.95. The ReLU function [13] is all replaced with Leaky-ReLU [42]. During training, the whole point cloud is flipped randomly along the X or Y axis, randomly rotated along the Z axis in the range $[-\pi/4, \pi/4]$ and translated by $[-0.5m, 0.5m]$, as well as globally scaled by a random factor sampled from [0.95, 1.05]. λ_1 , λ_2 , λ_3 are set to 1.0, 1.0 and 0.25, respectively. The inference time is measured on a 3070Ti GPU with batch size 1. On the nuScenes dataset, we set the detection range of the point cloud to $[-54m, 54m]$ for the X and Y axis and $[-5m, 3m]$ for the Z axis. For our FastPillars, we set the pillar size as 0.15m. Besides, following [47], we use the class-agnostic NMS with the score threshold set to 0.2 and rectification factor α to 0.5 for 10 classes during the post-processing in inference. For a fair comparison, we follow [30, 47] to only use double-flip test-time augmentation without any model ensemble on the nuScenes Dataset. Besides, we also use the ground-truth copy-paste data augmentation from [44] during training and disable this data augmentation in the last 5 epochs following [38] (e.g., using the fade strategy).

4.1. Overall Results

To better evaluate our method, we designed two quantitative experiments. We first quantitatively evaluated FastPillars on the nuScenes dataset `test` set with state-of-the-art methods. Then, we compared FastPillars with the real-time 3D detectors on the nuScenes datasets `val` set. Finally, we analyze the latency of each part of the model.

4.1.1 Quantitative Evaluation

For a fair comparison, we evaluate our FastPillars with previously published LiDAR-only non-ensemble methods on the nuScenes `test` set. As shown in Table 1, our FastPillars significantly outperform the state-of-the-art (SOTA) methods while having a real-time speed of 24FPS. Compared to the state-of-the-art method PillarNet [30],

Method	Stages	View	NDS(%)	mAP(%)	Car	Truck	Bus	Trailer	CV	Ped	Motor	BC	TC	Barrier
WYSIWYG [16]	One	BEV	41.9	35.0	79.1	30.4	46.6	40.1	7.1	65.0	18.2	0.1	28.8	34.7
PointPillars [20]	One	BEV	45.3	30.5	68.4	23.0	28.2	23.4	4.1	59.7	27.4	1.1	30.8	38.9
3DVID [46]	One	BEV	53.1	45.4	79.7	33.6	47.1	43.1	18.1	76.5	40.7	7.9	58.8	48.8
PointPainting [37]	One	58.1	46.4	77.9	35.8	36.2	37.3	15.8	73.3	41.5	24.1	62.4	60.2	
3DSSD [45]	One	Point	56.4	42.6	81.2	47.2	61.4	30.5	12.6	70.2	36.0	8.6	31.1	47.9
SSN [52]	One	BEV	58.1	46.4	80.7	37.5	39.9	43.9	14.6	72.3	43.7	20.1	54.2	56.3
Cylinder3D [53]	One	BEV	61.6	50.6	-	-	-	-	-	-	-	-	-	-
CBGS [51]	One	BEV	63.3	52.8	81.1	48.5	54.9	42.9	10.5	80.1	51.5	22.3	70.9	65.7
Pointformer [25]	One	Point	-	53.6	82.3	48.1	55.6	43.4	8.6	81.8	55.0	22.7	72.2	66.0
CVCNet [3]	One	BEV+RV	64.4	55.3	82.7	46.1	46.6	49.4	22.6	79.8	59.1	31.4	65.6	69.6
Centerpoint [47]	Two	BEV	65.5	58.0	84.6	51.0	60.2	53.2	17.5	83.4	53.7	28.7	76.7	70.9
FCOS-LIDAR [36]	One	RV	65.7	60.2	82.2	47.7	52.9	48.8	28.8	84.5	68.0	39.0	79.2	70.7
HotSpotNet [4]	One	BEV	66.0	59.3	83.1	50.9	56.4	53.3	23.0	81.3	63.5	36.6	73.0	71.6
VMVF [11]	One	BEV+RV	67.3	60.9	84.6	50.0	63.2	55.3	23.4	83.7	65.1	38.9	76.8	68.2
AFDetV2 [17]	One	BEV	68.5	62.4	86.3	54.2	62.5	58.9	26.7	85.8	63.8	34.3	80.1	71.0
VISTA-OHS [7]	One	BEV+RV	69.8	63.0	84.4	55.1	63.7	54.2	25.1	82.8	70.0	45.4	78.5	71.4
PillarNet-34 [†] [30]	One	BEV	71.2	65.8	87.5	58.0	65.3	63.9	28.8	87.4	68.0	40.0	82.2	76.9
FastPillars- <i>s</i> (Ours)	One	BEV	70.1	64.6	87.7	58.1	64.2	64.3	28.0	86.7	64.4	36.6	79.7	76.3
FastPillars- <i>m</i> (Ours)	One	BEV	71.0	65.8	88.0	60.3	67.5	64.3	29.9	87.3	66.1	38.0	82.5	74.6
FastPillars- <i>s</i> [‡] (Ours)	One	BEV	71.1	66.0	86.9	57.8	61.7	63.6	34.9	85.6	69.4	46.1	79.2	74.7
FastPillars- <i>m</i> [‡] (Ours)	One	BEV	71.8	66.8	87.3	58.0	66.0	62.3	34.5	87.4	70.3	47.9	81.5	72.8

Table 1. State-of-the-art comparisons for 3D detection on nuScenes test set. We show the NDS, and mAP for each class. Abbreviations: bird eye view (BEV), range view (RV), construction vehicle (CV), pedestrian (Ped), motorcycle (Motor), bicycle (BC) and traffic cone (TC). The table is mainly sorted by nuScenes detection score (NDS) which is the official ranking metric. [†]: reproduced based on official codebase. [‡]: add fade strategy on our method. The best results are marked in **bold** and second best results are marked in **blue** color.

Methods	SPCConv	FPS [†]	mAP% [†]	NDS% [†]	Pa.(M) [↓]	FLOPs(G) [↓]
PointPillars [‡] [19]	x	9	48.63	59.51	4.97	63.65
CP-PointPillars [‡] [19]	x	31	50.26	60.22	5.99	65.42
CP-VoxelNet [47]	✓	12	57.63	65.39	9.52	-
PillarNet-34 [†] [30]	✓	12	60.16	67.55	17.09	-
FastPillars- <i>s</i>	x	24	60.00	67.22	11.64	364.47
FastPillars- <i>m</i>	x	16	61.72	68.19	14.93	843.90

Table 2. The speed and accuracy comparison with the real-time one-stage methods on the nuScenes *val* set. [‡]: the results reported from PillarNet [30]. [†]: reproduced results based on the official codebase. For the method using SPCConv, the flops of the backbone is input-independent, so we did not report the flops results. The best results are marked in **bold** and the second best results are marked in **blue** color.

Method	FPS	Pillar/Voxel(ms)	Network(ms)	P-P(ms)	Overall(ms)
CenterPoint [47]	12.6	1.84	69.89	7.40	79.12
FastPillars- <i>s</i>	24.2	13.22	20.10	8.10	42.95
FastPillars- <i>m</i>	16.8	13.40	34.44	8.12	55.96

Table 3. **Inference time breakdowns.** We reported the time-consuming and overall speed of each part of our FastPillars-*s/m* models quantified by TensorRT with precision FP16. Abbreviations: Point-Encoding (PE), Post-processing (P-P).

FastPillars-*m* achieves almost the same performance and also surpasses almost all previous methods without the fade strategy. Note that both FastPillars and PillarNet make use

of the same training settings in the experiment. Particularly, compared with VISTA [7], the mAP/NDS of our FastPillars-*s*/FastPillars-*m* outperforms it 1.6%/2.8% and 0.3%/1.2% respectively. The performance of FastPillars-*s* and FastPillars-*m* could be further boosted by a substantial margin 1.4%/1.0% in mAP/NDS (from 64.6% to 66.0%/70.1% to 71.1%) and 1.0%/0.8% (from 65.8% to 66.8%/71.0% to 71.8%) with the fade strategy, respectively. The extensive experiments verify the excellent performance of FastPillars and its two variants (FastPillars-*s* and FastPillars-*m*), even without the use of sparse convolutions.

4.1.2 Comparisons with Real-time One-stage Methods

To further evaluate the speed and performance advantages of our method, we also compare FastPillars with real-time one-stage 3D point cloud detectors on the nuScenes *val* set. As shown in Table 2, compared with the PointPillars [20] implemented in the CenterPoint paper, which uses the training settings of CenterPoint, FastPillars-*s* also performs better by a margin of 9.74% and 7.0% in 3D mAP and NDS, respectively. Compared with the state-of-the-art method PillarNet [30], FastPillars-*s* achieves competitive performance (only 0.16% and 0.33% lower in mAP

Method	Lat (ms)	mAP(%) \uparrow	NDS(%) \uparrow	Car	Truck	Bus	Trailer	CV	Ped	Motor	BC	TC	Barrier
Att-pool	10.56	58.78	66.56	86.84	58.43	69.63	37.52	17.18	85.37	60.56	35.80	67.62	68.82
Max-pool	9.32	59.40	66.89	87.17	60.52	70.41	39.35	18.55	85.69	60.17	36.72	68.73	66.71
MAPE(ours)	13.22	60.00	67.22	86.90	58.21	72.59	37.67	17.68	86.08	60.24	40.36	70.06	70.15
		+0.60	+0.33	-0.27	-2.31	+2.18	-1.68	-1.87	+0.39	+0.07	+3.64	+1.33	+3.44

Table 4. Ablation experiments on the effect of Max-and-Attention Pillar Encoding (MAPE) module. Experiments show that our MAPE module can improve 0.6% map with ≈ 4 ms latency cost, especially for smaller objects such as the bicycle and barrier categories.

and NDS, respectively), but the speed is twice as fast as PillarNet. Experiments show our method has fewer parameters, higher performance and FPS. Note that FLOPs does not strongly reflect the real inference speed (*i.e.*, FPS). The significantly faster inference speed is due to the fact that PillarNet needs sparse convolutions, thus being not friendly to deployment, while our method is fully convolutional and can be effectively deployed in resource-restricted onboard systems with TensorRT and network quantization. Therefore, our method is able to provide a better trade-off between performance and speed.

4.1.3 Inference Time Analysis

As shown in Table 3. We use 10 sweeps of point cloud following the convention on the benchmark to measure the speed of FastPillars-*s/m* on nuScenes *test* set. Compared to CenterPoint, FastPillars-*s* achieves SOTA performance, improving CenterPoint by a margin of 2.37 mAP and 1.83 NDS, while running 2 \times faster in Tab. 2. The inference time of CenterPoint includes 1.84 ms for voxel encoding, 69.89 ms for network, and 7.40 ms for post-processing. FastPillars-*s* achieved 24 FPS on a single NVIDIA 3070Ti GPU, including 13.22 ms for pillar encoding, 20.10 ms for model forward propagation, and 8.10 ms for post-processing. For FastPillars-*m*, which has a bigger backbone, achieves 16.8 FPS on the same device, including 13.40 ms for pillar encoding, 34.44 ms for model forward propagation, and 8.12 ms for post-processing.

4.2. Ablation Experiments

Here, we conduct ablation studies for the MAPE module, multiple different lightweight networks and the Cross-Stage-Patral (CSP) ratios to analyze their influence on the speed and performance on the nuScenes *val* set.

4.2.1 Max-and-Attention Pillar Encoding Module

As shown in Table 4, compared with max-pooling operation, the MAPE module can boost 0.6% map performance improvement with only 4ms extra latency cost. To be specific, the mAP of the bicycle (BC), traffic cone (TC) and barrier categories are improved by 3.64%, 1.33% and

Ratio	mAP	NDS	Params	FLOPs	Latency
γ	\uparrow %	\uparrow %	\downarrow (M)	\downarrow (G)	\downarrow (ms)
0.3	57.95	65.69	1.62	94.65	11.76
0.5	59.40	66.89	2.55	171.83	12.37
0.7	59.32	66.90	3.86	279.62	18.78
0.8	59.67	67.21	4.69	350.81	21.11
0.9	60.49	67.62	5.63	428.52	21.84

Table 5. Ablation experiments on the different partial ratios of Cross-Stage-Patral network based on our CRVNet backbone. Lat means latency, the time is reported based quantified network on TensorRT with FP16 precision.

Backbone	mAP	NDS	Params	FLOPs	Lat
	\uparrow %	\uparrow %	\downarrow (M)	\downarrow (G)	\downarrow (ms)
Res34 [†]	60.04	67.63	8.97	561.30	21.93
Rep-Res34 [†]	59.93	67.37	9.98	627.97	21.61
CSP-Res34 [†]	59.24	66.80	3.26	168.32	13.50
CSPRep-Res34 [†]	59.37	66.22	3.60	187.50	13.66
RepVGG [†]	60.27	67.49	6.08	496.64	18.88
CSPRep-VGG [‡]	59.40	66.89	2.55	171.83	12.37
CSPRep-Res34 [‡]	61.32	67.88	6.17	706.80	26.72

Table 6. Ablation studies on the different lightweight backbone architectures on performance and latency. We provide various lightweight backbone network designs with the corresponding model parameters, performance and latency. Notably, only the backbone is changed and we keep other parts untouched to report the corresponding algorithm performance. [†]: means the raw block number setting, which is (4, 6, 16, 1) in VGG and (3, 4, 6, 3) in ResNet-34. [‡]: means our block number setting, which is (6, 16, 1, 1) in FastPillars-*s* and (6, 6, 3, 2) in FastPillars-*m*.

3.44% mAP, respectively, owing to the MAPE module. For pedestrian category, we conjecture their performance has saturated on the benchmark, so the MAPE module shows marginal improvement. The experiments show that our Max-and-Attention Pillar Encoding (MAPE) module encodes the local fine-grained geometrical patterns and the most prominent features (*i.e.*, the maximum value) effectively by combining the attentive-pooling and max-pooling operation, improving the perceptual ability for small size objects in the BEV perspective.

4.2.2 CSP Ratios Selection

We use different partial ratios of Cross-Stage-Patial network for ablation study based on our CRVNet backbone. As shown in Table 5, we find that when $\gamma = 0.5$, the performance of network outperforms $\gamma = 0.3$ 1.45% mAP with only 0.61ms latency. Although the mAP and NDS $\gamma = 0.9$ are 1.09 and 0.73 higher than at $\gamma = 0.5$, respectively, the time cost is almost twice that at $\gamma = 0.5$. One thing to be noted is that when γ increase from 0.5 to 0.8, the latency increases obviously, but the mAP only improved 0.27%. Therefore, we set $\gamma = 0.5$ in our network.

4.2.3 Lightweight Backbone Architecture

As shown in Table 6, we find that CSPRepVGG backbone applied to our FastPillars-*s* model has the smallest model capacity and latency while have a good performance with 59.40 mAP. CSPRep-Res34, which is our FastPillars-*m* model backbone, has the best performance despite having the largest parameter quantity and time-consuming. Compared with CSPRepVGG backbone, CSPRep-Res34 backbone performs better by a margin of 1.92 mAP and 0.99 NDS on nuScenes *val* set. Overall, our method achieves a good balance between speed and accuracy, especially has state-of-the-art performance with real-time latency.

5. Conclusion

In this paper, we propose **FastPillars**, a real-time one-stage pillar-based 3D detector, to simultaneously improve the detection accuracy and runtime efficiency while keeping the deployment in mind. In particular, we show that SPConv can be safely sidestepped with a redesigned powerful architecture. Moreover, we also propose a Max-and-Attention Pillar Encoding (MAPE) module to compensate for the information loss in the pillar encoding of PointPillars. Extensive experiments show that our FastPillars achieves a better trade-off between speed and accuracy, and can be quantitatively deployed through TensorRT for real-time on-device applications. Given its effectiveness and efficiency, we hope that our method can serve as a strong and simple alternative of current mainstream real-time SPConv-based 3D detectors.

References

- [1] Alexey Bochkovskiy, Chien-Yao Wang, and Hong-Yuan Mark Liao. Yolov4: Optimal speed and accuracy of object detection. *arXiv preprint arXiv:2004.10934*, 2020. 3
- [2] Holger Caesar, Varun Bankiti, Alex Lang, Sourabh Vora, Venice Erin Liang, Qiang Xu, Anush Krishnan, Yu Pan, Giancarlo Baldan, and Oscar Beijbom. Nuscenes: A multimodal dataset for autonomous driving. In *CVPR*, pages 11621–11631, 2020. 6
- [3] Qi Chen, Lin Sun, Ernest Cheung, Kui Jia, and Alan Yuille. Every view counts: Cross-view consistency in 3d object detection with hybrid-cylindrical-spherical voxelization. *NeurIPS*, 2020. 7
- [4] Qi Chen, Lin Sun, Zhixin Wang, Kui Jia, and Alan Yuille. Object as hotspots: An anchor-free 3d object detection approach via firing of hotspots. In *European conference on computer vision*, pages 68–84. Springer, 2020. 7
- [5] Xiaozihi Chen, Huimin Ma, Ji Wan, Bo Li, and Tian Xia. Multi-view 3D object detection network for autonomous driving. In *CVPR*, pages 1907–1915, 2017. 2
- [6] Jiajun Deng, Shaoshuai Shi, Peiwei Li, Wengang Zhou, Yanyong Zhang, and Houqiang Li. Voxel r-cnn: Towards high performance voxel-based 3D object detection. In *AAAI*, 2021. 1, 2, 5
- [7] Shengheng Deng, Zhihao Liang, Lin Sun, and Kui Jia. Vista: Boosting 3d object detection via dual cross-view spatial attention. In *Proceedings of the IEEE/CVF Conference on Computer Vision and Pattern Recognition*, pages 8448–8457, 2022. 7
- [8] Xiaohan Ding, Xiangyu Zhang, Ningning Ma, Jungong Han, Guiguang Ding, and Jian Sun. Repvgg: Making vgg-style convnets great again. In *Proceedings of the IEEE/CVF Conference on Computer Vision and Pattern Recognition*, pages 13733–13742, 2021. 3, 5
- [9] Mark Everingham, Luc Van Gool, Christopher KI Williams, John Winn, and Andrew Zisserman. The pascal visual object classes (voc) challenge. *IJCV*, 2010. 6
- [10] Lue Fan, Ziqi Pang, Tianyuan Zhang, Yu-Xiong Wang, Hang Zhao, Feng Wang, Naiyan Wang, and Zhaoxiang Zhang. Embracing single stride 3d object detector with sparse transformer. In *Proceedings of the IEEE/CVF Conference on Computer Vision and Pattern Recognition*, pages 8458–8468, 2022. 1
- [11] Hamidreza Fazlali, Yixuan Xu, Yuan Ren, and Bingbing Liu. A versatile multi-view framework for lidar-based 3d object detection with guidance from panoptic segmentation. In *Proceedings of the IEEE/CVF Conference on Computer Vision and Pattern Recognition*, pages 17192–17201, 2022. 7
- [12] Jocher Glenn. YOLOv5 release v6.1. <https://github.com/ultralytics/yolov5/releases/tag/v6.1>, 2022. 3
- [13] Xavier Glorot, Antoine Bordes, and Yoshua Bengio. Deep sparse rectifier neural networks. In *Proceedings of the fourteenth international conference on artificial intelligence and statistics*, pages 315–323. JMLR Workshop and Conference Proceedings, 2011. 6
- [14] Benjamin Graham and Laurens van der Maaten. Submanifold sparse convolutional networks. *arXiv preprint arXiv:1706.01307*, 2017. 1, 2, 5
- [15] Kaiming He, Xiangyu Zhang, Shaoqing Ren, and Jian Sun. Deep residual learning for image recognition. In *Proceedings of the IEEE conference on computer vision and pattern recognition*, pages 770–778, 2016. 5
- [16] Peiyun Hu, Jason Ziglar, David Held, and Deva Ramanan. What you see is what you get: Exploiting visibility for 3d object detection. *CVPR*, 2020. 7
- [17] Yihan Hu, Zhuangzhuang Ding, Runzhou Ge, Wenxin Shao, Li Huang, Kun Li, and Qiang Liu. Afdetv2: Rethinking the necessity of the second stage for object detection from point clouds. In *Proceedings of the AAAI Conference on Artificial Intelligence*, volume 36, pages 969–979, 2022. 6, 7
- [18] Hongwu Kuang, Bei Wang, Jianping An, Ming Zhang, and Zehan Zhang. Voxel-fpn: Multi-scale voxel feature aggregation for 3d object detection from lidar point clouds. *Sensors*, 20(3):704, 2020. 2
- [19] Alex H Lang, Sourabh Vora, Holger Caesar, Lubing Zhou, Jiong Yang, and Oscar Beijbom. Pointpillars: Fast encoders for object detection from point clouds. In *CVPR*, pages 12697–12705, 2019. 1, 2, 3, 4, 7
- [20] Alex H. Lang, Sourabh Vora, Holger Caesar, Lubing Zhou, Jiong Yang, and Oscar Beijbom. Pointpillars: Fast encoders for object detection from point clouds. *CVPR*, 2019. 7
- [21] Chuyi Li, Lulu Li, Hongliang Jiang, Kaiheng Weng, Yifei Geng, Liang Li, Zaidan Ke, Qingyuan Li, Meng Cheng, Weiqiang Nie, et al. Yolov6: a single-stage object detection framework for industrial applications. *arXiv preprint arXiv:2209.02976*, 2022. 3, 5
- [22] Tsung-Yi Lin, Piotr Dollár, Ross Girshick, Kaiming He, Bharath Hariharan, and Serge Belongie. Feature pyramid networks for object detection. In *Proceedings of the IEEE conference on computer vision and pattern recognition*, pages 2117–2125, 2017. 2
- [23] Tsung-Yi Lin, Priya Goyal, Ross Girshick, Kaiming He, and Piotr Dollár. Focal loss for dense object detection. In *Proceedings of the IEEE international conference on computer vision*, pages 2980–2988, 2017. 6
- [24] Daniel Maturana and Sebastian Scherer. Voxnet: A 3d convolutional neural network for real-time object recognition. In *2015 IEEE/RSJ international conference on intelligent robots and systems (IROS)*, pages 922–928. IEEE, 2015. 1
- [25] Xuran Pan, Zhuofan Xia, Shiji Song, Li Erran Li, and Gao Huang. 3d object detection with pointformer. In *Proceedings of the IEEE/CVF Conference on Computer Vision and Pattern Recognition*, pages 7463–7472, 2021. 7
- [26] Charles R Qi, Or Litany, Kaiming He, and Leonidas J Guibas. Deep hough voting for 3D object detection in point clouds. In *ICCV*, pages 9277–9286, 2019. 1
- [27] Charles R Qi, Wei Liu, Chenxia Wu, Hao Su, and Leonidas J Guibas. Frustum pointnets for 3D object detection from rgbd data. In *CVPR*, pages 918–927, 2018. 1
- [28] Charles R Qi, Hao Su, Kaichun Mo, and Leonidas J Guibas. Pointnet: Deep learning on point sets for 3D classification and segmentation. In *CVPR*, pages 652–660, 2017. 1

[29] Charles Ruizhongtai Qi, Li Yi, Hao Su, and Leonidas J Guibas. Pointnet++: Deep hierarchical feature learning on point sets in a metric space. In *NeurIPS*, pages 5099–5108, 2017. 1

[30] Guangsheng Shi, Ruiyang Li, and Chao Ma. Pillarnet: Real-time and high-performance pillar-based 3d object detection. In *ECCV*, 2022. 1, 2, 3, 5, 6, 7

[31] Shaoshuai Shi, Chaoxu Guo, Li Jiang, Zhe Wang, Jianping Shi, Xiaogang Wang, and Hongsheng Li. Pv-rcnn: Point-voxel feature set abstraction for 3D object detection. In *CVPR*, pages 10529–10538, 2020. 1

[32] Shaoshuai Shi, Xiaogang Wang, and Hongsheng Li. Pointrcnn: 3D object proposal generation and detection from point cloud. In *CVPR*, pages 770–779, 2019. 1

[33] Shaoshuai Shi, Zhe Wang, Jianping Shi, Xiaogang Wang, and Hongsheng Li. From points to parts: 3D object detection from point cloud with part-aware and part-aggregation network. *IEEE TPAMI*, 2020. 1

[34] Karen Simonyan and Andrew Zisserman. Very deep convolutional networks for large-scale image recognition. *arXiv preprint arXiv:1409.1556*, 2014. 3, 5

[35] Leslie N Smith and Nicholay Topin. Super-convergence: Very fast training of neural networks using large learning rates. In *Artificial intelligence and machine learning for multi-domain operations applications*, volume 11006, pages 369–386. SPIE, 2019. 6

[36] Zhi Tian, Xiangxiang Chu, Xiaoming Wang, Xiaolin Wei, and Chunhua Shen. Fully convolutional one-stage 3d object detection on lidar range images. *NeurIPS*, 2022. 5, 7

[37] Sourabh Vora, Alex H Lang, Bassam Helou, and Oscar Beijbom. Pointpainting: Sequential fusion for 3d object detection. *CVPR*, 2020. 7

[38] Chunwei Wang, Chao Ma, Ming Zhu, and Xiaokang Yang. Pointaugment: Cross-modal augmentation for 3d object detection. In *Proceedings of the IEEE/CVF Conference on Computer Vision and Pattern Recognition*, pages 11794–11803, 2021. 6

[39] Chien-Yao Wang, Alexey Bochkovskiy, and Hong-Yuan Mark Liao. Yolov7: Trainable bag-of-freebies sets new state-of-the-art for real-time object detectors. *arXiv preprint arXiv:2207.02696*, 2022. 3, 5

[40] Chien-Yao Wang, Hong-Yuan Mark Liao, Yueh-Hua Wu, Ping-Yang Chen, Jun-Wei Hsieh, and I-Hau Yeh. Cspnet: A new backbone that can enhance learning capability of cnn. In *Proceedings of the IEEE/CVF conference on computer vision and pattern recognition workshops*, pages 390–391, 2020. 3, 5

[41] Dominic Zeng Wang and Ingmar Posner. Voting for voting in online point cloud object detection. In *Robotics: Science and Systems*, pages 10–15607, 2015. 1

[42] Bing Xu, Naiyan Wang, Tianqi Chen, and Mu Li. Empirical evaluation of rectified activations in convolutional network. *arXiv preprint arXiv:1505.00853*, 2015. 6

[43] Shangliang Xu, Xinxin Wang, Wenyu Lv, Qinyao Chang, Cheng Cui, Kaipeng Deng, Guanzhong Wang, Qingqing Dang, Shengyu Wei, Yuning Du, et al. Pp-yoloe: An evolved version of yolo. *arXiv preprint arXiv:2203.16250*, 2022. 3, 5

[44] Yan Yan, Yuxing Mao, and Bo Li. Second: Sparsely embedded convolutional detection. *Sensors*, 18(10):3337, 2018. 1, 2, 5, 6

[45] Zetong Yang, Yanan Sun, Shu Liu, and Jiaya Jia. 3dssd: Point-based 3D single stage object detector. In *CVPR*, pages 11040–11048, 2020. 1, 7

[46] Junbo Yin, Jianbing Shen, Chenye Guan, Dingfu Zhou, and Ruigang Yang. Lidar-based online 3d video object detection with graph-based message passing and spatiotemporal transformer attention. *CVPR*, 2020. 7

[47] Tianwei Yin, Xingyi Zhou, and Philipp Krahenbuhl. Center-based 3d object detection and tracking. In *CVPR*, pages 11784–11793, 2021. 1, 2, 3, 5, 6, 7

[48] Zhaohui Zheng, Ping Wang, Wei Liu, Jinze Li, Rongguang Ye, and Dongwei Ren. Distance-iou loss: Faster and better learning for bounding box regression. In *Proceedings of the AAAI conference on artificial intelligence*, volume 34, pages 12993–13000, 2020. 6

[49] Yin Zhou and Oncel Tuzel. Voxelnet: End-to-end learning for point cloud based 3D object detection. In *CVPR*, pages 4490–4499, 2018. 1, 2

[50] Benjin Zhu, Zhengkai Jiang, Xiangxin Zhou, Zeming Li, and Gang Yu. Class-balanced grouping and sampling for point cloud 3d object detection. *arXiv preprint arXiv:1908.09492*, 2019. 6

[51] Benjin Zhu, Zhengkai Jiang, Xiangxin Zhou, Zeming Li, and Gang Yu. Class-balanced grouping and sampling for point cloud 3d object detection. *arXiv:1908.09492*, 2019. 7

[52] Xinge Zhu, Yuexin Ma, Tai Wang, Yan Xu, Jianping Shi, and Dahu Lin. Ssn: Shape signature networks for multi-class object detection from point clouds. *ECCV*, 2020. 7

[53] Xinge Zhu, Hui Zhou, Tai Wang, Fangzhou Hong, Wei Li, Yuexin Ma, Hongsheng Li, Ruigang Yang, and Dahu Lin. Cylindrical and asymmetrical 3d convolution networks for lidar-based perception. *IEEE Transactions on Pattern Analysis and Machine Intelligence*, 2021. 7

A. Visualization on nuScenes Dataset

Some visualization results are shown in Fig. 4. Here, we visualize the detection results in some challenging scenarios on the nuScenes *val* set based on our FastPillars-*s* model. As we can see, FastPillars can work reliably under a wide variety of challenging circumstances. We can clearly see that the proposed FastPillars is capable of detecting small targets, such as pedestrians, barriers and bicycles.

B. Ablation Experiments of Different Pooling Operation in MAPE

We compare the performance of different pooling operations in Tab. 7. The results show the combination of Atten+Max pooling in MAPE has the best performance. The reason is that MAPE module encodes the local geometrical patterns automatically and the most prominent features (*i.e.*, the maximum value) effectively by combining the attentive-pooling and max-pooling operation.

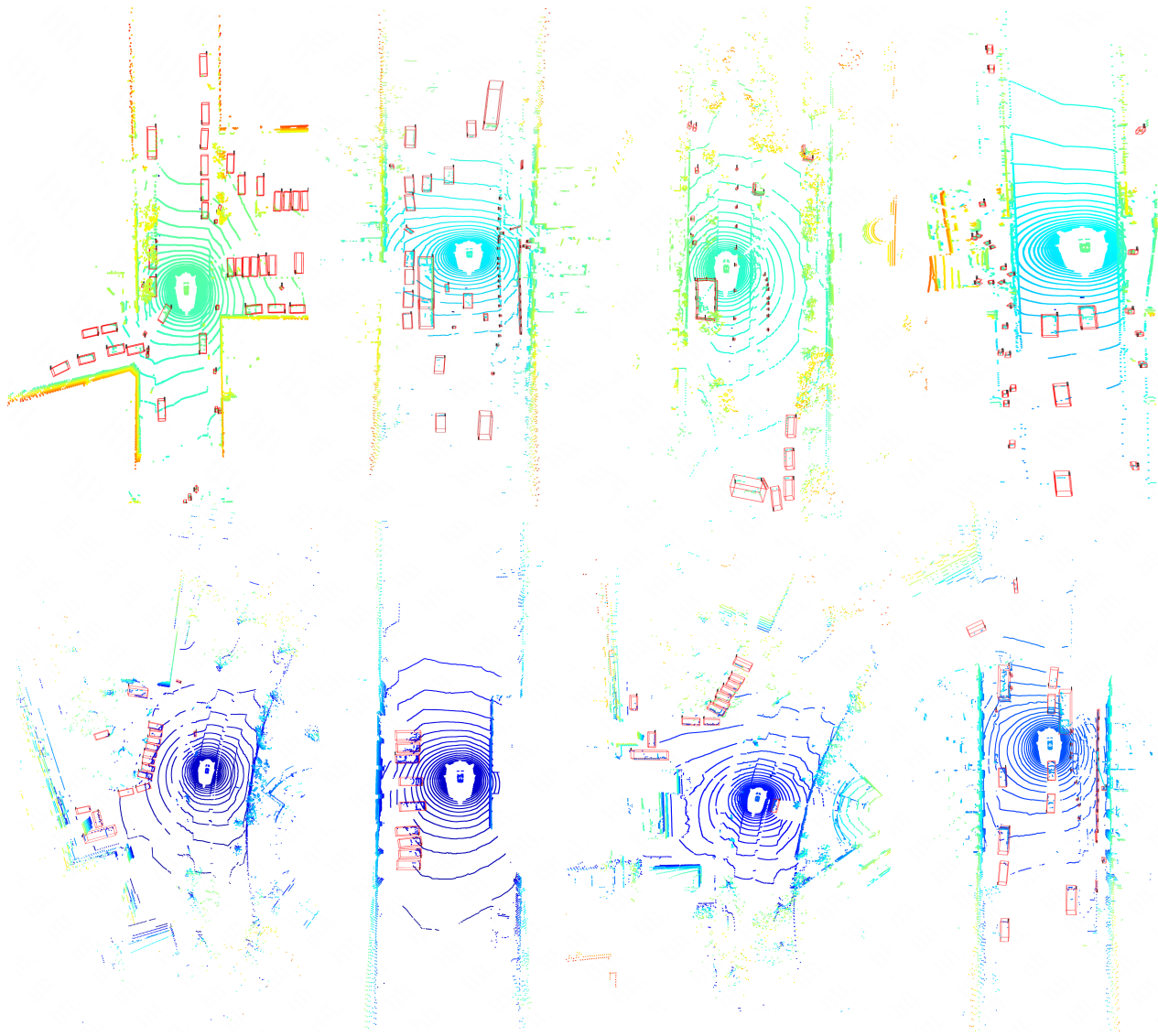


Figure 4. Visualization results of FastPillars on the nuScenes *val* set.

Method	mAP(%) \uparrow	Car	Truck	Bus	Trailer	CV	Ped	Motor	BC	TC	Barrier
Avg-pool	57.85	86.67	58.23	69.74	37.25	15.73	84.89	57.35	30.72	67.71	70.14
Atten-pool	58.78	86.84	58.43	69.63	37.52	17.18	85.37	60.56	35.80	67.62	68.82
Max-pool	59.40	87.17	60.52	70.41	39.35	18.55	85.69	60.17	36.72	68.73	66.71
Max+Avg-pool	58.19	86.58	56.57	70.97	38.33	15.02	85.22	58.28	33.55	67.82	69.59
Avg+Atten-pool	59.45	86.87	58.69	70.82	38.13	17.09	85.59	60.25	37.80	70.01	69.23
MAPE(ours)	60.00	86.90	58.21	72.59	37.67	17.68	86.08	60.24	40.36	70.06	70.15
	+0.60	-0.27	-2.31	+2.18	-1.68	-1.87	+0.39	+0.07	+3.64	+1.33	+3.44

Table 7. Additional ablations of MAPE.